

Viruslike Nanoparticles with Maghemite Cores Allow for Enhanced MRI Contrast Agents

Andrey G. Malyutin,[†] Rosemary Easterday,[†] Yaroslav Lozovyy,[†] Alessandro Spilotros,[‡] Hu Cheng,[§] Olivia R. Sanchez-Felix,[†] Barry D. Stein,[†] David Gene Morgan,[†] Dmitri I. Svergun,[‡] Bogdan Dragnea,^{*,†} and Lyudmila M. Bronstein^{*,†,‡}

[†]Department of Chemistry, Indiana University, 800 East Kirkwood Avenue, Bloomington, Indiana 47405, United States

[‡]European Molecular Biology Laboratory (EMBL), Hamburg Outstation, Notkestraße 85, D-22603 Hamburg, Germany

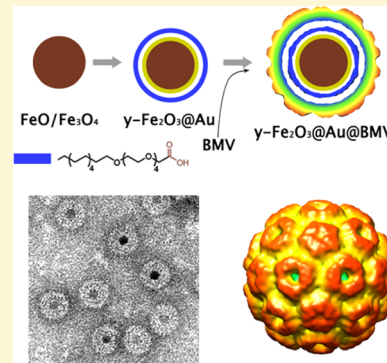
[§]Department of Psychological and Brain Sciences, Indiana University, 1101 East Tenth Street, Bloomington, Indiana 47403, United States

[†]Department of Biology, Indiana University, 1001 East Third Street, Bloomington, Indiana 47405, United States

[#]Department of Physics, Faculty of Science, King Abdulaziz University, Jeddah, Saudi Arabia

S Supporting Information

ABSTRACT: Here, for the first time, we demonstrate formation of virus-like nanoparticles (VNPs) utilizing gold-coated iron oxide nanoparticles as cores and capsid protein of brome mosaic virus (BMV) or hepatitis B virus (HBV) as shells. Further, utilizing cryo-electron microscopy and single particle methods, we are able to show that the BMV coat on VNPs assembles into a structure very close to that of a native virion. This is a consequence of an optimal iron oxide NP size (~ 11 nm) fitting the virus cavity and an ultrathin gold layer on the maghemite cores, which allows for utilization of $\text{SH}-(\text{CH}_2)_{11}-(\text{CH}_2-\text{CH}_2-\text{O})_4-\text{OCH}_2-\text{COOH}$ as capping molecules to provide sufficient stability, charge density, and small form factor. MRI studies show unique relaxivity ratios that diminish only slightly with gold coating. A virus protein coating of a magnetic core mimicking the wild-type virus makes these VNPs a versatile platform for biomedical applications.



INTRODUCTION

Viruses are nature's quintessential delivery vectors. Their highly evolved mechanisms for infecting cells and improved current understanding of their life cycles have resulted in recombinant viruses as prime vectors for shuttling exogenous DNA in a variety of types of cells and for gene therapy in selected applications.^{1,2} Innate biocompatibility, tissue tropism, narrow size distribution, possibilities of direct chemical or genetic engineering, and the ability to produce them in reasonable amounts represent a set of desirable properties for nanomedicine applications hard to emulate in synthetic vectors.^{3–9} Besides biomedical applications, virus shells devoid of their genomes have been explored as vessels for coupled reactions, to grow and organize extended nanoparticle (NP) systems, employed as scaffolds to produce electrodes, and as systems for light harvesting applications.^{10–18}

Another area where virus-based materials show promise is as contrast agents for magnetic resonance imaging (MRI) when paired with superparamagnetic particles or ions. Primary agents currently used in clinical setting are longitudinal (T_1) contrast agents based on Gd(III), which is heavily chelated to minimize toxic side-effects.¹⁹ Viruslike particles containing multiple Gd(III) ions were reported elsewhere.²⁰ An alternative exists in the form of superparamagnetic iron oxide NPs, which act as

transverse (T_2) contrast agents.^{21,22} Iron oxide is nontoxic, as it can be metabolized by a body, and more abundant than gadolinium.^{23,24} Several MRI contrast agents based on iron oxide NPs have been already approved by FDA.²⁵

Iron oxide NPs can be prepared in a range of shapes and sizes to tune their MR response. The challenge, however, lies in making these particles biocompatible and/or recognized by certain cells or organs. For biocompatibility, a range of approaches has been previously examined such as coating with chitosan, diblock copolymers, and PEGylated phospholipids.^{26–28} An advantageous alternative, however, might lie in employing regular viral coats to stabilize iron oxide NPs, increase circulation time, and to help target cells of interest.

In all these nanotechnology applications, in particular in the synthesis of superparamagnetic core VNPs, the viral characteristics to be preserved in the hybrid are embodied in the protein shell structure. Determining whether the cargo–shell interaction influences the structure of the protein shell and thus may affect its properties is crucial. Because of their straightforward scale, shape, and surface chemistry control, gold nanoparticles

Received: October 31, 2014

Revised: December 12, 2014

Published: December 15, 2014

have provided an initial suitable model to explore the interaction between cargo and the virus protein shell.^{29–32} However, because of much stronger scattering from the metal core with respect to the protein shell, for structural analysis, one is restricted to negative stain transmission electron microscopy, which is limited by stain diffusion and dehydration artifacts.

Previously, we have adapted the templated assembly method to form magnetic VNPs based on superparamagnetic, MR active FeO/Fe₃O₄ NPs that were functionalized with negatively charged PEGylated phospholipids (2000 Da PEG) followed by encapsulation by brom mosaic virus (BMV) proteins.^{33,34} It was shown that the FeO/Fe₃O₄ NPs are a promising *T*₂ MRI contrast agent and could be potentially useful as a way to track systemic movement of VNPs in plants. However, steric effects in PEGylated phospholipids preclude reaching sufficient charge densities on the surface of the small NPs, and encapsulation by this method is limited to significantly larger cores than the inner diameter of the virus, which may impact native interactions and thus function.^{33,34}

To overcome these limitations, in this work, we have developed a novel method, which is not limited in the size of the cores, and thus smaller, maghemite (γ -Fe₂O₃) NP cores, commensurate with the virus inner cavity, could be utilized. Maghemite NP cores have a large *T*₂ MRI response and, as it will be shown here, produce VNPs that maintain the native capsid structure. To achieve suitable interactions with the protein shell, 11 nm maghemite NPs were coated with an ultrathin gold layer. Several other groups have previously coated Fe₃O₄ and γ -Fe₂O₃ particles with gold shells.^{35–39} However, in our case, thick gold layers would increase the scattering cross-section for electrons which is detrimental to cryo-TEM. Furthermore, it could deteriorate the MRI contrast added by the NPs by increasing the distance between water protons and the magnetic core or by disrupting the magnetic core spin structure.³⁷

For functionalization of the thin gold layer the versatile gold–thiol chemistry can be utilized. To achieve optimal charge density the ligand used was SH-(CH₂)₁₁-(CH₂-CH₂-O)₄-OCH₂-COOH (SH-PEG-COOH), same as previously used with gold NPs for VNP synthesis.^{29,30,32} The approach reported here, with its lower electron scattering cores, allowed for the first time structural analysis of inorganic core VNPs by cryo-electron microscopy. The maghemite NPs demonstrated high relaxivity ratios indicating an excellent potential as a *T*₂ contrast agent. Versatility of the approach was confirmed by extending it to the human hepatitis B virus (HBV).

EXPERIMENTAL SECTION

Materials and Methods. **Materials.** FeCl₃·6H₂O (98%), oleylamine (70%), gold(III) chloride hydrate (99%), octadecane (99%), Trizma base (99.9%), cesium chloride (98%), and magnesium acetate tetrahydrate (99%) were purchased from Sigma-Aldrich and used as received. Potassium chloride (99%), sodium citrate dehydrate (99%), and sodium chloride (99%) were purchased from Mallinckrodt chemicals and used as received. Magnesium chloride 6-hydrate (99%) was purchased from J.T. Baker and used as received. Hexanes (85%), ethanol (95%), acetone (99.8%), sodium acetate anhydrous (99%), and sodium phosphate monobasic monohydrate (98%) were from EMD and used as received. Chloroform (Mallinckrodt, 100%), oleic acid (TCI, 95%), and oleic acid sodium salt (ScienceLab.com, 95%) were used without purification. SH-(CH₂)₁₁-(CH₂-CH₂-O)₄-OCH₂-COOH was acquired from ProChimia Surfaces.

Virus Preparation. BMV was expressed via *Agrobacterium*-mediated gene delivery method in *Nicotinia benthamiana*. Plants were allowed to grow for 7 days post infection. The leaves were then collected and homogenized in virus buffer (0.25 M NaOAc, 0.01 M MgCl₂, pH 4.5). The slurry was then centrifuged on a Beckman TA-10.250 rotor at 5000 rpm for 25 min. The supernatant was then centrifuged on a Beckman SW32 rotor for 3 h at 26 000 rpm on a 10% sucrose cushion. The pellet was resuspended in 38.5% CsCl and the virus band was isolated by centrifugation for 24 h on a Beckman TL-71 rotor at 45 000 rpm. The band was dialyzed against SAMA buffer (0.05 M NaOAc, 0.008 M Mg(OAc)₂, pH 4.5), with 3 changes. The virus was further purified by FPLC equipped with a Superose-6 column. Virus was disassembled and RNA precipitated by dialysis against disassembly buffer (0.5 M CaCl₂, pH 7.4), with three changes of the buffer. RNA was removed by centrifugation on a Beckman TLA 110 rotor at 35 000 rpm for 30 min. The supernatant protein dimers were dialyzed against Tris (0.01 M Tris, pH 7.4) buffer and then TNKM (0.05 M Tris, 0.05 M NaCl, 0.01 M KCl, 0.005 M MgCl₂, pH 7.4) for 24 h each.

Hepatitis B expression is explained in detail elsewhere.⁴⁰ Briefly, full capsid protein sequence with C-terminal domain codon optimized for expression in *E. coli* were used for HBV protein expression. Cells were lysed by sonication and HBV capsids were isolated by centrifugation. Capsids were further purified by size exclusion chromatography and stored at -80 °C until needed.

Synthesis of Iron Oxide Nanoparticles. NPs of 10.7 nm in diameter were prepared via thermal decomposition of iron oleate as described elsewhere.⁴¹ Briefly, in a typical experiment, 1.92 g of iron oleate complex, 1.54 mL oleic acid, and 5.27 g of octadecane were placed in a three-neck round-bottom flask (with elongated necks) equipped with a magnetic stir bar, a reflux condenser, and two septa, one of which contains an inserted temperature probe protected with a glass shield. The reaction solution was heated to 60 °C to melt octadecane and allow dissolution of the components under stirring. Then, the temperature was increased to 318 °C at 2.2 °C/min. Upon reaching 318 °C, the solution was refluxed for 20 min, cooled to room temperature, and stored at 4 °C.

Oxidation of Iron Oxide Nanoparticles. The reaction solution was melted with a heat gun and transferred to a three-neck round-bottom flask described above. The solution was heated in air at 5 °C/min to reach 200 °C and the temperature was maintained for 2 h. The solution was allowed to cool to room temperature. About 1 mL of solution was withdrawn and NPs were precipitated with a mixture of 1 mL of hexane and 4 mL of acetone and separated by 15 min centrifugation. Washing was repeated twice with the same mixture and the NPs after the final centrifugation were resuspended in chloroform.

Gold Coating of Iron Oxide Nanoparticles. Gold coating was carried out by a modified procedure described elsewhere.⁴² In a typical experiment, a solution containing 4 mg of γ -Fe₂O₃ NPs, 1 mL chloroform, and 0.8 mL of oleylamine was prepared and allowed to stir for 1 h. Following this, 0.0985 g of HAuCl₄·H₂O was combined with 0.2 mL of oleylamine and 1 mL of chloroform. The resultant solution was added dropwise to the NP containing solution and allowed to stir for 24 h. The sample was purified by precipitation in ethanol followed by centrifugation and removal of the supernatant and then washed twice with a mixture of 5:1 ethanol:hexane. Following this the NPs were dissolved in chloroform. A calibration curve showing absorbance (at 300 nm) vs NP concentration in chloroform was obtained. The data were linearly fitted and the slope value (12.95 cm² mg⁻¹) was used as the extinction coefficient to determine the NP concentration in the following experiments.

PEGylation of Gold-Coated Iron Oxide Nanoparticles. A solution of 1 mg of γ -Fe₂O₃@Au in 1 mL of chloroform was prepared in a vial. The NP solution was added to a calculated amount of a SH-PEG-COOH ligand, ~7 ligands per nm² of surface area of NPs, and allowed to stir for 24 h.³¹ Following this, the chloroform was removed in vacuum and 1 mL of deionized water was added to the vial. The aqueous mixture was sonicated briefly and then left stirring for 24 h. The aggregates (if any) were removed by 15 min centrifugation at 3000 rpm and supernatant was purified by ultracentrifugation at 40 000 rpm for 15 min.

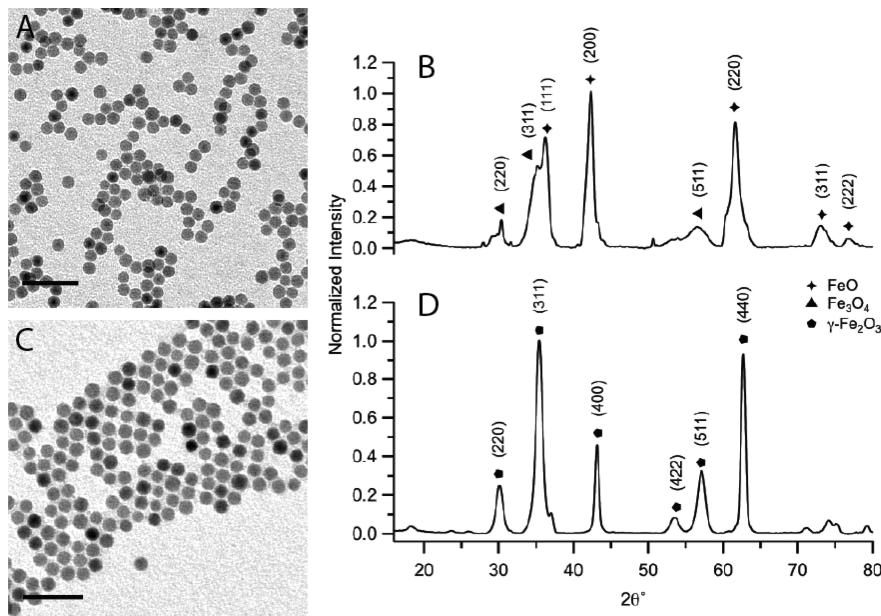


Figure 1. (A) TEM image and (B) XRD profile of as-synthesized $\text{FeO}/\text{Fe}_3\text{O}_4$ NPs. (C) TEM image and (D) XRD profile of $\gamma\text{-Fe}_2\text{O}_3$ NPs. Scale bars are 50 nm.

BMV VNP Assembly. $\gamma\text{-Fe}_2\text{O}_3@\text{Au}$ VNPs were prepared as previously reported for gold core VNPs.²⁹ Briefly, NPs and BMV dimers are mixed at a ratio of 1 to 99 in TNKM buffer (0.05 M Tris-HCl, 0.05 M NaCl, 0.01 M KCl, 0.005 M MgCl_2) to make a solution volume of 100 μL at the protein concentration of 0.5 mg/mL. The solution was dialyzed in TNKM for 24 h. The mixture was then dialyzed again at pH 4.6 and low ionic strength SAMA buffer (0.05 M NaOAc, 0.008 M Mg(OAc)_2).

HBV VNP Assembly. Viral capsids, composed of full length protein subunits and random *E. coli* RNA, were dialyzed against 1.5 M guanidine HCl buffer (0.5 M LiCl, 50 mM HEPES, 2 mM DTT, pH 7.5) to disassemble the capsids into dimers and precipitate the RNA. The RNA was then removed by centrifugation, and the protein dimers were further purified by HPLC. The dimers were then mixed with the $\gamma\text{-Fe}_2\text{O}_3@\text{Au}$ NPs at the same ratio as used with BMV proteins and dialyzed against low ionic strength buffer (0.1 M NaCl, 50 mM Tris, pH 7.5).

Characterization. *X-ray Photoelectron Spectroscopy.* X-ray photoelectron spectroscopy measurements were performed on the PHI Versa Probe II instrument equipped with monochromatic Al K(α) source. The experiments were run at the base pressure ca. $4-8 \times 10^{-10}$ Torr. In all experiments, the X-ray power of 65 W at 15 kV was used with beam size of 260 μm at take off angles of 45°. Utilizing the Fermi edge of the valence band for metallic silver for XPS and UPS (Hell line), the instrumental resolution was determined to be 0.3 and 0.15 eV respectively. Minimums of 10–60 scans were collected for the spectra, using 0.05–0.1 eV step and 23 eV pass energy. The spectra were recorded using SmartSoft-XPS v2.0 (PHI) and processed using MultiPack v9.0 (PHI) and/or CasaXPS v2.3.14. Curve-fitting was performed with Shirley background. The instrument was calibrated to give a binding energy of 84.0 eV for Au 4f_{7/2} line as well as BE's of 284.8, 932.7, and 368.3 eV for the C 1s line of adventitious (aliphatic) carbon presented on the nonsputtered samples, for Cu 2p_{3/2} and for Ag 3d_{5/2} photoemission lines, respectively.

ζ -Potential and DLS Measurements. ζ -potential and DLS measurements were performed on Malvern Zetasizer Nano ZS. For the DLS measurements, the sample was diluted in 18.2 MΩ water and the data from at least three measurements were averaged. Intensity and volume distributions of the particle sizes were recorded. The ζ -potential was measured at pH 7.4. The data were processed using the absorption of bulk iron oxide, the indices of refraction of iron oxide and solvent, and the viscosity of the pure water. The Smoluchowski

approximation was used to convert the electrophoretic mobility to a ζ -potential.

Fourier Transform Infrared Spectroscopy. FTIR spectra were recorded on a Nicolet spectrometer. The samples were prepared by evaporating the chloroform solutions of NPs on the KBr disk.

Thermal Gravimetric Analysis. TGA was performed on TGAQ5000 IR manufactured by TA Instruments. The TGA samples were prepared by evaporation of NPs solutions in 100 μL platinum pans, by filling the pan and allowing chloroform to evaporate. The experiments were carried upon heating to 700 °C with a rate 10.0 °C/min.

(Cryo) Electron Microscopy. Grids for electron microscopy were prepared by applying four microliters of sample to a freshly glow discharged, in-house prepared continuous carbon film on a 200 mesh copper grid. For nanoparticle samples in chloroform, no blotting or staining was necessary. Aqueous samples were blotted after 30s, followed by 10s staining with 4 μL drop of 3% uranyl acetate. Images were acquired on a JEOL JEM1010 at accelerating voltage of 80 kV.

To prepare samples for cryo-em, four microliters of sample were applied to holey carbon grids (Quantifoil 2/2, Quantifoil Micro Tools) at 6 °C and 100% RH. Grids were blotted and vitrified by plunging into liquid ethane using Vitrobot Mark III (FEI) and stored in liquid nitrogen until examined using a JEOL JEM 3200FS operating at 300 kV. Images were acquired using a Gatan Ultrascan 4000 CCD camera under low dose conditions of $\sim 18 \text{ e}^-/\text{\AA}^2$.

The BMV VNP cryo-em images were preprocessed using EMAN2.⁴³ Supervised automated particle selection of EMAN2 was used to acquire ~ 17000 particles from ~ 280 micrographs. This data set was further manually screened and only cores with continuous, spherical protein shells were kept, resulting in ~ 7000 particles. The entire set was then processed by Auto3dEM, using a random initial model generated by the package and imposed icosahedral geometry.⁴⁴ Concurrently, particles were classified with RELION into 20 classes.^{45,46} Class averages were screened by Igor Pro to measure core and shell sizes. An improved structure was obtained by utilizing Auto3dEM to reconstruct only class#15 with 520 particles.

Small-Angle X-ray Scattering. Synchrotron SAXS measurements were performed at the European Molecular Biology Laboratory (EMBL) on the storage ring DORIS III of the Deutsches Elektronen Synchrotron (DESY, Hamburg) on the P12 beamline equipped with a robotic sample changer and a 2 M PILATUS detector (DECTRIS, Switzerland). Samples were measured at 10 °C in a concentration

range 0.5–2.0 mg/mL. The scattering was recorded in the range of the momentum transfer $0.07 < s < 4.5 \text{ nm}^{-1}$, where $s = (4\pi \sin \theta)/\lambda$, 2θ is the scattering angle, and $\lambda = 0.12 \text{ nm}$ is the X-ray wavelength. The measurements were carried out in a vacuum capillary; no measurable radiation damage was detected by comparison of ten successive time frames with 100 ms exposures. The experimental scattering profiles from all solutes were corrected for the background scattering from the appropriate solvent and processed using standard procedures.⁴⁷ The concentration dependence was absent for all solutes, and the highest concentration data were used for further analysis. The radius of gyration R_g and the maximum particle dimension D_{\max} were evaluated using the program GNOM.⁴⁸ All SAXS patterns were analyzed with the routine MIXTURE within the software suite PRIMUS.⁴⁷ Polydisperse core–shell spheres were used to fit the data, the radius and the polydispersity of cores and shells of the particles defined by a monomodal Gaussian distribution were parametrized. Interparticle interactions within the approximation of sticky hard sphere potential were taken into account that allowed us to fit the scattering at low angles ($s < 0.15 \text{ nm}^{-1}$).

Magnetic Resonance Imaging. The T1 and T2 relaxation times (s) were measured with a 3 T TIM Trio magnetic resonance imaging (MRI) scanner (Siemens Medical Solutions, Erlangen, Germany). For T1 relaxation time measurement, a series of T1-weighted images were obtained using turbo spin echo sequence with inversion recovery. TR/TE = 15000/10 ms, TI = 100, 200, 400, 800, 1600, 3200, 4000, 5000, 6000, 10000, flip angle = 180°. Turbo factor = 7, slice thickness = 2 mm, in-plane resolution = 0.935 mm × 0.935 mm. The voxel-wised image intensity S with respect to different TI were fit to eq 1 using least-squares curve fitting to obtain the T1 value.

$$S = M_0 |1 - 2e^{-TI/T1} + e^{-TR/T1}| \quad (2)$$

For T2 relaxation time measurement, a series of T2-weighted images were obtained with spin echo sequence. TR = 4000 ms, TE = 11, 22, 44, 88, 160, 240 ms, flip angle = 90°. Slice thickness = 3 mm, in-plane resolution = 1.875 mm × 1.875 mm. The voxel-wised image intensity S with respect to different TE were fit to eq 2 using least-squares curve fitting to obtain the T2 value.

$$S = M_0 e^{-TE/T2} \quad (3)$$

RESULTS AND DISCUSSION

Oxidation of FeO/Fe₃O₄ NPs. Iron oxide NPs prepared by thermal decomposition of iron oleate are shown in Figure 1A.⁴¹ They are spherical, 10.7 nm in diameter, with ~7% size polydispersity. The X-ray powder diffraction (XRD) pattern from these NPs (Figure 1B) demonstrates the presence of reflections representative for wüstite (FeO) and spinel, which can be magnetite (Fe₃O₄) or maghemite (γ -Fe₂O₃) (the two forms are indistinguishable because of line broadening). However, considering anaerobic synthesis conditions, the spinel phase is likely to be Fe₃O₄ (Figure 1B).^{49,50}

These NPs were first employed for gold coating using a procedure described elsewhere.⁴² However, in these initial attempts no detectable coverage was found presumably due to the dense coating by OA of the NP surface. Further, preferential binding of gold to maghemite over magnetite has been previously shown.³⁶ Thus, we carried oxidation of the reaction solution of the FeO/Fe₃O₄ NPs in air at 200 °C for 2 h. The TEM image and XRD pattern of the oxidized NPs are presented in Figure 1C, D. The reflections match the spinel structure, which in this case, is most likely γ -Fe₂O₃ because of oxidative environment.⁵⁰

FTIR and TGA characterization suggested (see the Supporting Information, SI) that the density of the OA residues on the NP surface decreased upon oxidation which improved the likelihood of a successful Au coating.

Gold-Coated γ -Fe₂O₃ NPs and Their Functionalization.

NP templates of ~11 nm only were utilized to minimize any morphological variations from the native capsid structure of the protein shell. The total diameter of the NP coated with a ligand could not exceed the inner cavity of BMV, about 18 nm. Additionally, previous work has shown optimal assembly with gold NPs of ~12 nm in diameter.³⁰ Based on these criteria, NPs of 10.7 nm in diameter were selected for gold and protein coating.

Figure 2A shows no significant changes to NP shape or size after oxidation (γ -Fe₂O₃ NPs) or gold coating (γ -Fe₂O₃@Au

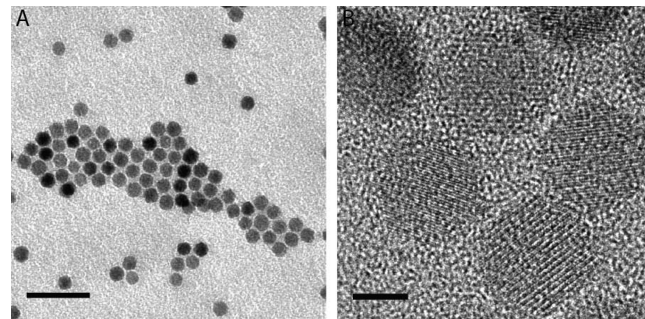


Figure 2. (A) TEM and (B) high-resolution TEM images of γ -Fe₂O₃@Au NPs. Scale bars are 50 and 5 nm, respectively.

NPs). γ -Fe₂O₃@Au NPs became water-soluble after coating with the HOOC-PEG-SH, strongly indicating that gold coating did take place. An identical procedure applied to γ -Fe₂O₃ NPs induces no change in the hydrophobic nature of the NPs. However, the gold shell was too thin to be detectable by HRTEM (Figure 2B).

Presence of a gold layer was confirmed by X-ray photoelectron spectroscopy (XPS) (Figure 3). At the beginning of the data acquisition, gold peaks are dominating (Figure 3C). Then, as the Ar ion beam sputters away the top surface layer, the intensity of the gold peaks decreases while the peaks corresponding to iron oxide become dominant (Figure 3B, C). These results point to a gold layer a few atomic layers thick.

The hydrodynamic diameter of the γ -Fe₂O₃@Au NPs coated with HS-PEG-COOH, obtained from DLS measurements, is 21 nm (Figure 4). This value is in a good agreement with the expected 25 nm diameter obtained from the 10.7 nm cores plus the estimated fully extended length, ~7 nm, of HS-PEG-COOH.⁵¹ The ζ -potential is -38.4 mV somewhat larger than that of gold NPs functionalized in the similar manner (~ -32 mV for 12 nm gold particles). Further, this ζ -potential surpasses -22.8 and -32.8 mV of 8.5 and 20.1 nm, respectively, of iron oxide NPs coated with anionic PEGylated phospholipids.³³ The high ζ -potential value of the γ -Fe₂O₃@Au NPs is crucial because the NP cores should possess a certain charge density to be successfully coated with virus proteins.⁵²

BMV and HBV Protein Assembly around HS-PEG-COOH-Functionalized γ -Fe₂O₃@Au NPs. As was shown before, the BMV coat protein can self-assemble around a variety of negatively charged templates.^{29,30,34} BMV shells can also form on cores that far exceed the size of BMV inner cavity.^{33,34} The VNP structure in this case, although potentially approximating locally that of larger icosahedral capsids, is likely misshapen and defect ridden.^{53,54} In contrast, 12 nm gold NPs formed well-defined VNPs, capable of cocrystallizing with

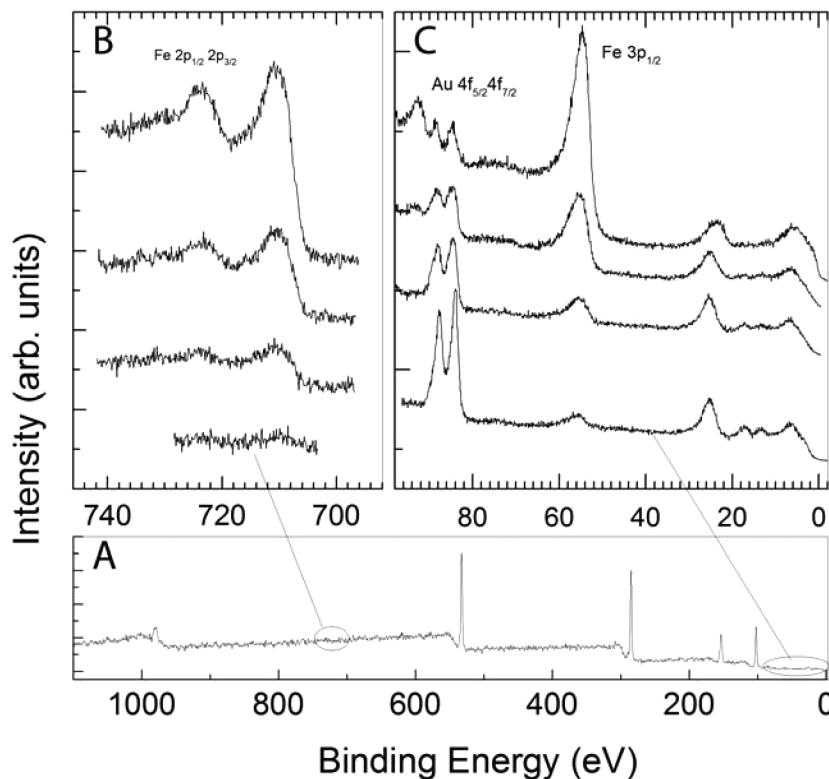


Figure 3. (A) Survey XPS spectra of $\gamma\text{-Fe}_2\text{O}_3@\text{Au}$ nanoparticles. High-resolution XPS spectra of (B) Fe 2p and (C) Au 4f, Fe 3p and valence band region upon Ar sputtering. Sputtering dose increases from the bottom to the top.

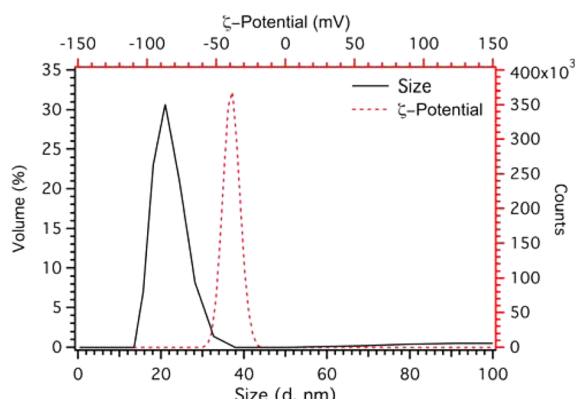


Figure 4. Hydrodynamic diameter (black solid trace) and ζ -potential (red dashed trace) of the HS-PEG-COOH coated $\gamma\text{-Fe}_2\text{O}_3@\text{Au}$ NPs.

native BMV, suggesting VNP shells that are nearly identical in structure with the wild-type virus.³⁰

Figure 5A shows the TEM image of the VNPs formed with the $\gamma\text{-Fe}_2\text{O}_3@\text{Au}$ cores stained with uranyl acetate. The small dark circles are the $\gamma\text{-Fe}_2\text{O}_3@\text{Au}$ NPs, the inner lighter ring around the NPs is the SH-PEG-COOH layer, and the final gray ring is the BMV protein layer. The diameter of VNPs is \sim 28 nm, which matches the diameter of a native BMV. Assembly efficiency, calculated as the ratio of well-defined VNPs to the total number of NPs was found to be 71.5%. This efficiency exceeds that of iron oxide cores functionalized with PEGylated phospholipids and nearly matches that of gold NPs functionalized with SH-PEG-COOH at equivalent protein concentration.^{31,33} The hydrodynamic diameter of the VNPs obtained from DLS measurements (see Figure S2 in the Supporting Information) was 38 nm, indicating the presence of VNP

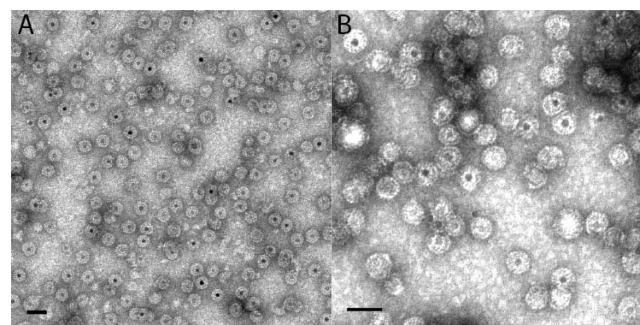


Figure 5. TEM images of $\gamma\text{-Fe}_2\text{O}_3@\text{Au}$ NPs encapsulated in the (A) BMV and (B) HBV capsid proteins. The TEM grid is negatively stained with uranyl acetate. Scale bars are 50 nm.

dimers. The ζ -potential, measured in SAMA buffer (0.05 M NaOAc, 0.008 M Mg(OAc)₂) at pH 4.5 was found to be 22 mV (see Figure S2 in the Supporting Information). This value is in agreement with the 14 mV value of VNPs with pure gold cores measured in same conditions.

To show that the approach is not restricted to simple icosahedral plant viruses for which BMV is a model, we have also examined the ability of the nucleocapsid of HBV, a human virus, to encapsulate $\gamma\text{-Fe}_2\text{O}_3@\text{Au}$ NPs. Although these VNPs lack the membrane and glycoproteins found on the native HBV virus and, hence the virulence, HBV VNPs could be chemically or genetically modified to induce *in vitro* targeting specificity to certain cell types.⁵⁵ Figure 5B shows assembled HBV VNPs. Assembly efficiency was somewhat lower than that of BMV VNPs (60.2%). HBV purified from cells is predominantly T=4, but a small subpopulation of T = 3 capsids also occurs. The TEM-measured VNP average size is 33 nm, which is equivalent

to $T = 4$ HBV capsids.⁵⁴ Although assembly of HBV VNPs around gold cores has been previously reported by He et al.,⁵⁴ to the best of our knowledge, this is the first example of magnetic HBV VNPs that can be prospective MRI contrast agents employed in mammalian systems.

Small-Angle X-ray Scattering Characterization. To measure the radial density distribution function of BMV VNPs, we characterized assembled VNPs, gold-coated $\gamma\text{-Fe}_2\text{O}_3$ cores, and native BMV particles by SAXS. Scattering patterns are presented in Figure 6 (dots with experimental error bars).

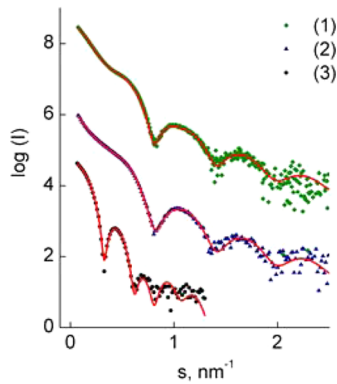


Figure 6. SAXS scattering patterns (dots with experimental error bars) for VNPs (curve 1), $\gamma\text{-Fe}_2\text{O}_3$ @Au NPs (curve 2), and BMV particles (curve 3). The fits (solid curves) were obtained using the polydisperse core–shell sphere model by the program MIXTURE. The plot displays the logarithm of the scattering intensity as a function of momentum transfer $s = 4\pi \sin(\theta)/\lambda$, where θ is the scattering angle and $\lambda = 0.12$ nm is the X-ray wavelength. Curves are displaced with respect to each other by one logarithmic order for better visualization.

All curves display oscillations with alternating minima/maxima typical for spherical particles. The shapes of the maxima/minima are rather symmetric for $\gamma\text{-Fe}_2\text{O}_3$ @Au and BMV data, whereas it becomes more broad and asymmetric for VNPs. For both $\gamma\text{-Fe}_2\text{O}_3$ @Au NPs and VNPs, the cutoff at $s_{\min} = 0.8$ nm⁻¹ was sufficient to remove the influence of the interparticle interactions (association) and to evaluate the characteristics of the individual particles. The average radii of gyration R_g and the maximum sizes D_{\max} of individual $\gamma\text{-Fe}_2\text{O}_3$ @Au NPs, VNPs and BMV particles as estimated from the program GNOM are summarized in Table 1. These sizes correlate well with the data

Table 1. Characteristic Sizes of the Particles Derived from SAXS Data Using the Program GNOM

sample	R_g^a (nm)	D_{\max}^b (nm)
VNP	4.6 ± 0.2	12.5 ± 0.5
$\gamma\text{-Fe}_2\text{O}_3$ @Au	4.4 ± 0.2	11.5 ± 0.5
BMV	10.1 ± 0.3	28.0 ± 1.0

^a R_g is the radius of gyration; ^b D_{\max} is the maximum particle size.

obtained by TEM measurements. One has to note that for VNPs, the core part ($\gamma\text{-Fe}_2\text{O}_3$ @Au NPs) has significantly larger electron density than the shell part (composed of BMV capsids) therefore the effective maximum size of the particle (calculated by GNOM in the approximation of homogeneous particles) will be lower than the actual size of BMV capsids. To get the actual size characteristics of the VNPs, we employed the polydisperse core–shell sphere model that allowed us to fit the data (Figure 6, solid curves) and to determine the core/shell

radii and their polydispersities (Table 2). It was found that the inner (core) radii of VNPs and of $\gamma\text{-Fe}_2\text{O}_3$ @Au NPs are equal

Table 2. Structural Parameters of the Particles Obtained from a Polydisperse Core–Shell Sphere Model

sample	R_{core}^a (nm)	ΔR_{core}^b (nm)	R_{shell}^c (nm)	$\Delta R_{\text{shell}}^d$ (nm)
VNP	5.4 ± 0.2	0.3 ± 0.1	14.1 ± 0.5	1.2 ± 0.2
$\gamma\text{-Fe}_2\text{O}_3$ @Au	5.5 ± 0.2	0.3 ± 0.1		
BMV	4.8 ± 0.3	0.3 ± 0.1	13.2 ± 0.5	0.3 ± 0.1

^a R_{core} is the radius of the core (inner) part of the sphere; ^b ΔR_{core} is the polydispersity degree of the core part; ^c R_{shell} is the outer radius of the protein shell; ^d ΔR_{shell} is the polydispersity degree of the shell.

to 5.5 nm and are comparable with the radius of the hollow part of the BMV capsid, whereas the outer (shell) part of the VNP is equal to 14 nm and is compatible with the outer radius of the BMV capsid. Both the inner and the outer parts of the VNPs have moderate degree of polydispersity (0.33 nm for the core and 1.2 nm for the shell). The obtained structural parameters are in good agreement with TEM data (Figures 2 and 5). Attractive interparticle interactions that led to the scattering intensity increase at low angles ($s < 0.8$ nm⁻¹) for the $\gamma\text{-Fe}_2\text{O}_3$ @Au and VNP solutions can be described in terms of sticky hard sphere potential (the sticky parameter τ was found to be equal to 0.1). One cannot also exclude the formation of the associates (consisting of 2–5 individual particles) in the $\gamma\text{-Fe}_2\text{O}_3$ @Au and VNP solutions that are in dynamic equilibrium.

Cryo-EM Studies. To further characterize VNPs, we carried out single particle reconstruction from vitrified particles. Figure 7A shows a representative image of the frozen sample. Utilizing the best 7000 particles, the model produced (~16.5 Å at FSC 0.5, Figure 7B) is nearly identical to the native BMV structure in 8C (filtered to 15 Å). However, as was shown by Sun et al., the VNP structure is highly dependent on the core size.³⁰ Class averages, produced by RELION, were then analyzed by measuring core and shell sizes. Two of the classes are shown in Figure 7D, the entire set is shown in Figure S3 in the Supporting Information. Classification result set core diameter range from 9.5 to 11.8 nm and protein shell diameter range from 24.2 to 27.8 nm. Each class, ranging from ~200 to ~600 particles was independently processed using Auto3dDEM. Two of the classes (15 and 18) having core diameters of ~10 nm produced the BMV-like structure without supplying an initial model. One of the structures generated from class 15 (see Figure S3 in the Supporting Information) is shown in Figure 7E. It is an improvement compared to the initial structure acquired from the entire set (Figure 7B), as contributions from particles with very different core and protein shell diameters were removed from reconstruction.

MRI Measurements. To evaluate the effects of oxidation and gold coating on the MRI properties of iron oxide NPs, we investigated MR relaxivities and map images of the $\gamma\text{-Fe}_2\text{O}_3$ NPs and the $\gamma\text{-Fe}_2\text{O}_3$ @Au cores. Experiments were performed in a clinical 3T MR scanner at room temperature. The qualitative dependences of T_1 and T_2 relaxation times on nanoparticle and VNP concentrations are shown in Figure 8 and Figure S4 (Supporting Information). In both T_1 and T_2 maps, the dose-dependent contrast change is clearly observed.

To quantitatively compare the samples, inverse relaxation times ($1/T_{n(\text{samples})} - 1/T_{n(\text{solvent})}$, where n is 1 or 2) were plotted as a function of iron concentration (Figure 9). The slopes of the fits were used to calculate the longitudinal r_1 and transverse

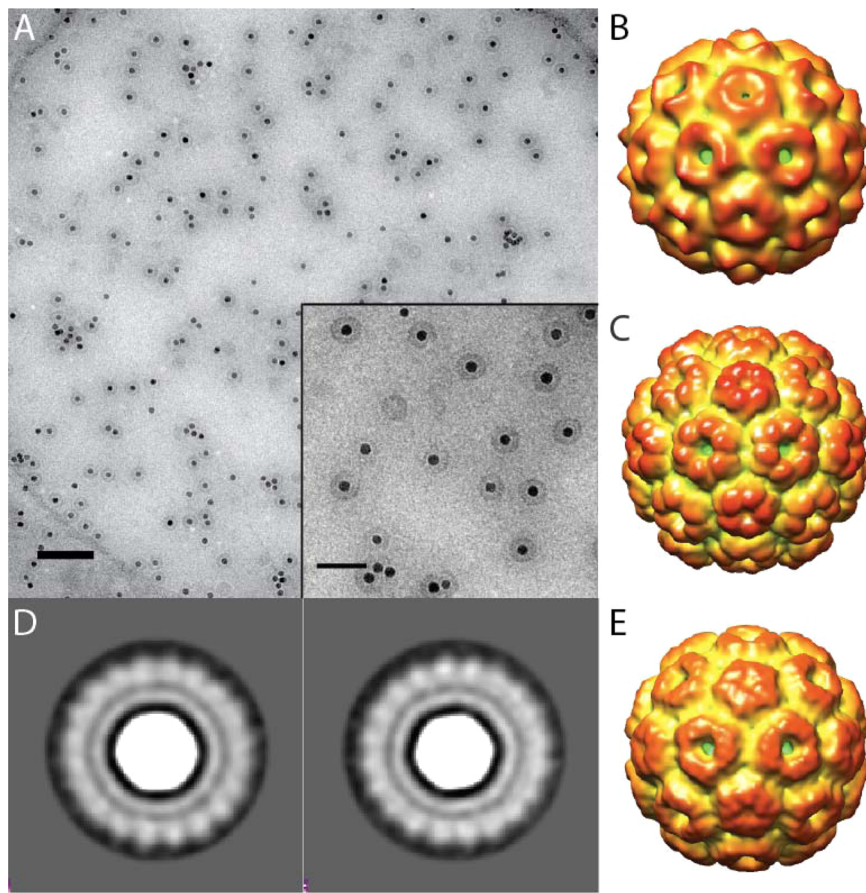


Figure 7. (A) Frozen hydrated image of VNP particles (100 nm scale bar) (inset: zoomed in view of the VNP particles, 50 nm scale bar). (B) $\sim 16.5 \text{ \AA}$ resolution reconstruction from 7000 particles. (C) BMV structure acquired by X-ray crystallography filtered to 15 \AA resolution. (D) Class averages showing features in the protein density. (E) VNP reconstruction from subset of classes.

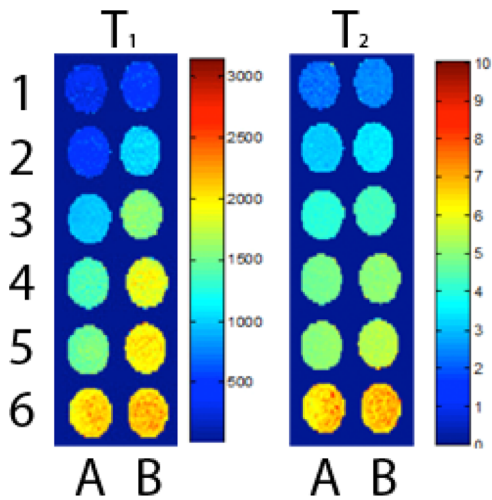


Figure 8. Longitudinal T_1 map and transverse T_2 map of 10.7 nm $\gamma\text{-Fe}_2\text{O}_3@\text{Au}$ NPs (A) and 10.6 nm $\gamma\text{-Fe}_2\text{O}_3$ NPs (B). Scale bar in the T_1 map is linear, whereas in the T_2 map, it is logarithmic. Sample concentrations: (1) 1.86, (2) 0.74, (3) 0.28, (4) 0.12, (5) 0.08, and (6) 0.02 mM Fe.

r_2 relaxivities, and the r_2/r_1 ratio can be used to compare the effectiveness of T2 contrast agents. As can be seen in Table 3, the r_2/r_1 ratio of $\gamma\text{-Fe}_2\text{O}_3@\text{Au}$ NPs dropped slightly, compared to that of 11 nm $\gamma\text{-Fe}_2\text{O}_3$ NPs as a result of gold coating. The change is not due to the significant decreased in r_2 value but to

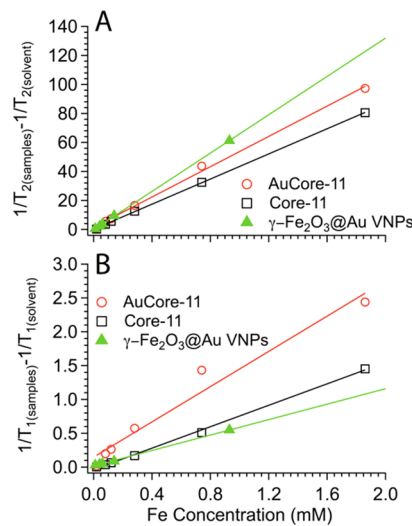


Figure 9. Plots of inverse relaxation times (A) ($1/T_{1(\text{samples})}-1/T_{1(\text{solvent})}$) and (B) ($1/T_{2(\text{samples})}-1/T_{2(\text{solvent})}$) as a function of iron concentration. The slopes correspond to (A) the longitudinal r_1 and (B) the transverse r_2 relaxivities, respectively.

the nearly doubled r_1 value. Nonetheless, the r_2/r_1 ratio for the $\gamma\text{-Fe}_2\text{O}_3@\text{Au}$ NPs was significantly higher compared to that of contrast agents that are in clinical use and gold-coated iron oxide NPs reported by others (Table 3).²⁵

Table 3. MRI Characteristics of the NPs Reported in This Papers and Other Selected Examples from Literature

sample	size D (nm)	r_1 ($\text{mM}^{-1} \text{s}^{-1}$)	r_2 ($\text{mM}^{-1} \text{s}^{-1}$)	r_2/r_1
$\gamma\text{-Fe}_2\text{O}_3$	10.6	0.79	43.3	54.8
$\gamma\text{-Fe}_2\text{O}_3@\text{Au}$	10.7	1.30	52.2	40.1
$\gamma\text{-Fe}_2\text{O}_3@\text{Au BMV VNP}$	10.7/28	0.57	66.0	115.8
Feridex	120–180	23.9	98.3	4.1
Resovist	60	25.4	151.0	5.9
Ferumoxtran-10	28	10	60	6.0
$\text{Fe}_3\text{O}_4@\text{Au}@\text{Glu}^{38}$	6.1	10	160	16.0
$\text{Au}@\text{MnFe}_2\text{O}_4^{57}$	12	6.01	83.3	13.9

Surprisingly, upon coating of $\gamma\text{-Fe}_2\text{O}_3@\text{Au}$ with BMV protein shell, the r_2/r_1 ratio nearly triples to 115.8 (Figure 9 and Table 3). The r_1 value decreases to 0.57, below that of the $\gamma\text{-Fe}_2\text{O}_3$ NPs, probably as a result of the increase in the local viscosity around the particles because of the protein coat, reducing a vibrational motion of the water molecules. The r_2 value is increased relative to both oxidized and gold coated NPs. This is likely a result of the decreased diffusion of NPs upon increasing in size and mass after encapsulation with the protein shell.

$$r_2 = \frac{1}{T_2} = \frac{a}{d_{\text{NP}} D} \gamma^2 \mu^2 C_{\text{NP}} J(\omega, \tau_D) \quad (1)$$

where a is the constant, d_{NP} is the NP diameter, D is the diffusion coefficient, μ is the NP magnetic moment, γ is the gyromagnetic ratio of the water proton; C_{NP} is the NP concentration, and $J(\omega, \tau_D)$ is the spectral density function.⁵⁶ Indeed, the dominant parameter in eq 1 thought to vary most between VNPs and $\gamma\text{-Fe}_2\text{O}_3@\text{Au}$ cores is the diffusion coefficient D .

We believe that significantly higher relaxivity ratios reported here (relative to other $\text{Fe}_3\text{O}_4@\text{Au}$ particles, Table 3) are due to an ultrathin layer of gold that does not disrupt the magnetic core spin structure.

CONCLUSION

$\gamma\text{-Fe}_2\text{O}_3$ NPs of 10.7 nm were coated with an ultrathin gold layer and further functionalized with the HS-PEG-COOH ligand. Functionalized NPs were encapsulated in BMV capsid proteins to form well-defined VNPs with high encapsulation efficiency. This approach simplifies and expands the arsenal of preparation methods for biomimetic magnetic NPs. The resulting VNPs maintained the same size as the native virus, as determined by TEM and SAXS. For the first time, it was possible to perform cryo-electron microscopy on VNPs to obtain the native protein shell structure that was found to be similar to the wild-type virus as determined by single particle reconstruction. The $\gamma\text{-Fe}_2\text{O}_3@\text{Au}$ VNPs showed excellent MRI response as a T_2 -weighted contrast agent. Because of their biomimetic properties such particles could prove important for investigating viral trafficking in host plants using MRI. Approach versatility was demonstrated by extending it to an animal virus.

ASSOCIATED CONTENT

Supporting Information

Description of FTIR, TGA, DLS, ζ -potential, MR maps of VNPs, and cryo-EM class data. This material is available free of charge via the Internet at <http://pubs.acs.org>.

AUTHOR INFORMATION

Corresponding Authors

*E-mail: dragnea@indiana.edu.

*E-mail: lybronst@indiana.edu.

Author Contributions

The manuscript was written through contributions of all authors.

Notes

The authors declare no competing financial interest.

ACKNOWLEDGMENTS

This work has been supported, in part, by the U.S. Department of Energy, Office of Science, Basic Energy Sciences, under Award DE-SC0010507 and Human Frontier Science Program research grant RGP0017/2012. We thank the IU Nanoscale Characterization Facility and the IU imaging facility at the Department of Psychological and Brain Sciences for access to the instrumentation. We also thank the lab of Dr. Adam Zlotnick for providing us with HBV coat protein.

REFERENCES

- Burton, E. A.; Fink, D. J.; Glorioso, J. C. *DNA Cell Biol.* **2002**, *21*, 915–936.
- Asokan, A.; Samulski, R. J. *Nat. Biotechnol.* **2006**, *24*, 158–160.
- Fields, B. N.; Knipe, D. M.; Howley, P. M. *Fields' Virology*; Wolters Kluwer Health/Lippincott Williams & Wilkins: Alphen aan de Rijn, South Holland, 2007.
- Porta, C.; Spall, V. E.; Loveland, J.; Johnson, J. E.; Barker, P. J.; Lomonosoff, G. P. *Virology* **1994**, *202*, 949–955.
- Lomonosoff, G. P., Virus particles and the uses of such particles in bio- and nanotechnology. In *Recent Advances in Plant Virology*; Caister Academic Press: Norfolk, U.K., 2011; pp 363–385.
- Gillitzer, E.; Willits, D.; Young, M.; Douglas, T. *Chem. Commun.* **2002**, 2390–2391.
- Douglas, T.; Young, M. *Science* **2006**, *312*, 873–875.
- Steinmetz, N. F. *Nanomed.-Nanotechnol.* **2010**, *6*, 634–641.
- Ho, M.; Judd, J.; Kuypers, B.; Yamagami, M.; Wong, F.; Suh, J. *Cell. Mol. Bioeng.* **2014**, *1*–10.
- Douglas, T.; Young, M. *Nature* **1998**, *393*, 152–155.
- Royston, E.; Ghosh, A.; Kofinas, P.; Harris, M. T.; Culver, J. N. *Langmuir* **2008**, *24*, 906–912.
- Lewis, J. D.; Destito, G.; Zijlstra, A.; Gonzalez, M. J.; Quigley, J. P.; Manchester, M.; Stuhlmann, H. *Nat. Med.* **2006**, *12*, 354–360.
- Dixit, S. K.; Goicochea, N. L.; Daniel, M.-C.; Murali, A.; Bronstein, L.; De, M.; Stein, B.; Rotello, V. M.; Kao, C. C.; Dragnea, B. *Nano Lett.* **2006**, *6*, 1993–1999.
- de la Escosura, A.; Nolte, R. J. M.; Cornelissen, J. J. L. M. *J. Mater. Chem.* **2009**, *19*, 2274–2278.
- Dedeo, M. T.; Finley, D. T.; Francis, M. B. *Prog. Mol. Biol. Transl. Sci.* **2011**, *103*, 353–392.
- Steinmetz, N. F.; Manchester, M. *Viral Nanoparticles: Tools for Materials Science and Biomedicine*; Pan Stanford Publishing: Singapore, 2011; p 1–273.
- Chen, P. Y.; Dang, X. N.; Klug, M. T.; Qi, J. F.; Courchesne, N. M. D.; Burpo, F. J.; Fang, N.; Hammond, P. T.; Belcher, A. M. *ACS Nano* **2013**, *7*, 6563–6574.
- Kostiainen, M. A.; Hiekataipale, P.; Laiho, A.; Lemieux, V.; Seitsonen, J.; Ruokolainen, J.; Ceci, P. *Nat. Nanotechnol.* **2013**, *8*, 52–56.

- (19) Port, M.; Idée, J.-M.; Medina, C.; Robic, C.; Sabatou, M.; Corot, C. *BioMetals* **2008**, *21*, 469–490.
- (20) Smith, G. R.; Xie, L.; Lee, B.; Schwartz, R. *Biophys. J.* **2014**, *106*, 310–320.
- (21) Weissleder, R.; Elizondo, G.; Wittemberg, J.; Rabito, C. A.; Bengele, H. H.; Josephson, L. *Radiology* **1990**, *175*, 489–493.
- (22) Ito, A.; Shinkai, M.; Honda, H.; Kobayashi, T. *J. Biosci. Bioeng.* **2005**, *100*, 1–11.
- (23) Schlachter, E. K.; Widmer, H. R.; Bregy, A.; Lonnfors-Weitzel, T.; Vajtai, I.; Corazza, N.; Bernau, V. J.; Weitzel, T.; Mordasini, P.; Slotboom, J.; Herrmann, G.; Bogni, S.; Hofmann, H.; Frenz, M.; Reinert, M. *Int. J. Nanomed.* **2011**, *6*, 1793–1800.
- (24) Hentze, M. W.; Muckenthaler, M. U.; Galy, B.; Camaschella, C. *Cell* **2010**, *142*, 24–38.
- (25) Wang, Y. X. *Quan. Imaging Med. Surg.* **2011**, *1*, 35–40.
- (26) Pellegrino, T.; Manna, L.; Kudera, S.; Liedl, T.; Koktysh, D.; Rogach, A. L.; Keller, S.; Raedler, J.; Natile, G.; Parak, W. J. *Nano Lett.* **2004**, *4*, 703–707.
- (27) Shtykova, E. V.; Huang, X.; Remmes, N.; Baxter, D.; Stein, B.; Dragnea, B.; Svergun, D. I.; Bronstein, L. M. *J. Phys. Chem. C* **2007**, *111*, 18078–18086.
- (28) Shtykova, E. V.; Huang, X.; Gao, X.; Dyke, J. C.; Schmucker, A. L.; Dragnea, B.; Remmes, N.; Baxter, D. V.; Stein, B.; Konarev, P. V.; Svergun, D. I.; Bronstein, L. M. *J. Phys. Chem. C* **2008**, *112*, 16809–16817.
- (29) Chen, C.; Daniel, M.-C.; Quinkert, Z. T.; De, M.; Stein, B.; Bowman, V. D.; Chipman, P. R.; Rotello, V. M.; Kao, C. C.; Dragnea, B. *Nano Lett.* **2006**, *6*, 611–615.
- (30) Sun, J.; DuFort, C.; Daniel, M.-C.; Murali, A.; Chen, C.; Gopinath, K.; Stein, B.; De, M.; Rotello, V. M.; Holzenburg, A.; Kao, C. C.; Dragnea, B. *Proc. Natl. Acad. Sci. U.S.A.* **2007**, *104*, 1354–1359.
- (31) Daniel, M.-C.; Tsvetkova, I. B.; Quinkert, Z. T.; Murali, A.; De, M.; Rotello, V. M.; Kao, C. C.; Dragnea, B. *ACS Nano* **2010**, *4*, 3853–3860.
- (32) Tsvetkova, I.; Chen, C.; Rana, S.; Kao, C. C.; Rotello, V. M.; Dragnea, B. *Soft Matter* **2012**, *8*, 4570–4576.
- (33) Huang, X.; Bronstein, L. M.; Retrum, J.; Dufort, C.; Tsvetkova, I.; Aniagyei, S.; Stein, B.; Stucky, G.; McKenna, B.; Remmes, N.; Baxter, D.; Kao, C. C.; Dragnea, B. *Nano Lett.* **2007**, *7*, 2407–2416.
- (34) Huang, X.; Stein, B. D.; Cheng, H.; Malyutin, A.; Tsvetkova, I. B.; Baxter, D. V.; Remmes, N. B.; Verchot, J.; Kao, C.; Bronstein, L. M.; Dragnea, B. *ACS Nano* **2011**, *5*, 4037–4045.
- (35) Chen, M.; Yamamoto, S.; Farrell, D.; Majetich, S. A. *J. Appl. Phys.* **2003**, *93*, 7551–7553.
- (36) Lyon, J. L.; Fleming, D. A.; Stone, M. B.; Schiffer, P.; Williams, M. E. *Nano Lett.* **2004**, *4*, 719–723.
- (37) Gallo, J.; Garcia, I.; Padro, D.; Arnaiz, B.; Penades, S. *J. Mater. Chem.* **2010**, *20*, 10010–10020.
- (38) Carril, M.; Fernandez, I.; Rodriguez, J.; Garcia, I.; Penades, S. *Part. Part. Syst. Charact.* **2014**, *31*, 81–87.
- (39) Wagstaff, A. J.; Brown, S. D.; Holden, M. R.; Craig, G. E.; Plumb, J. A.; Brown, R. E.; Schreiter, N.; Chrzanowski, W.; Wheate, N. *J. Inorg. Chim. Acta* **2012**, *393*, 328–333.
- (40) Porterfield, J. Z.; Dhason, M. S.; Loeb, D. D.; Nassal, M.; Stray, S. J.; Zlotnick, A. *J. Virol.* **2010**, *84*, 7174–7184.
- (41) Bronstein, L. M.; Huang, X.; Retrum, J.; Schmucker, A.; Pink, M.; Stein, B. D.; Dragnea, B. *Chem. Mater.* **2007**, *19*, 3624–3632.
- (42) Xu, Z.; Hou, Y.; Sun, S. *J. Am. Chem. Soc.* **2007**, *129*, 8698–8699.
- (43) Tang, G.; Peng, L.; Baldwin, P. R.; Mann, D. S.; Jiang, W.; Rees, I.; Ludtke, S. *J. Struct. Biol.* **2007**, *157*, 38–46.
- (44) Yan, X.; Sinkovits, R. S.; Baker, T. S. *J. Struct. Biol.* **2007**, *157*, 73–82.
- (45) Scheres, S. H. W. *J. Mol. Biol.* **2012**, *415*, 406–418.
- (46) Scheres, S. H. W. *J. Struct. Biol.* **2012**, *180*, 519–530.
- (47) Konarev, P. V.; Volkov, V. V.; Sokolova, A. V.; Koch, M. H. J.; Svergun, D. I. *J. Appl. Crystallogr.* **2003**, *36*, 1277–1282.
- (48) Svergun, D. I. *J. Appl. Crystallogr.* **1992**, *25*, 495–503.
- (49) Bronstein, L. M.; Huang, X.; Retrum, J.; Stein, B.; Remmes, N. B.; Baxter, D. V.; Dixit, S.; Dragnea, B. *Polym. Prepr. (Am. Chem. Soc., Div. Polym. Chem.)* **2006**, *47*, 849–850.
- (50) Hou, Y.; Xu, Z.; Sun, S. *Angew. Chim. Int. Ed.* **2007**, *46*, 6329–6332.
- (51) Hong, R.; Fischer, N. O.; Verma, A.; Goodman, C. M.; Emrick, T.; Rotello, V. M. *J. Am. Chem. Soc.* **2004**, *126*, 739–743.
- (52) Zhou, H.-X. *FEBS Lett.* **2013**, *587*, 1053–1061.
- (53) Zandi, R.; Reguera, D.; Bruinsma, R. F.; Gelbart, W. M.; Rudnick, J. *Proc. Natl. Acad. Sci. U. S. A.* **2004**, *101*, 15556–15560.
- (54) He, L.; Porterfield, Z.; van der Schoot, P.; Zlotnick, A.; Dragnea, B. *ACS Nano* **2013**, *7*, 8447–8454.
- (55) Nishimura, Y.; Mimura, W.; Mohamed Suffian, I. F.; Amino, T.; Ishii, J.; Ogino, C.; Kondo, A. *J. Biochem. (Tokyo, Jpn.)* **2013**, *153*, 251–256.
- (56) Na, H. B.; Song, I. C.; Hyeon, T. *Adv. Mater. (Weinheim, Ger.)* **2009**, *21*, 2133–2148.
- (57) Ahmad, T.; Iqbal, Y.; Bae, H.; Rhee, I.; Hong, S.; Chang, Y.; Lee, J. *J. Korean Phys. Soc.* **2013**, *62*, 1696–1701.